Journal of Materials Chemistry A

Accepted Manuscript

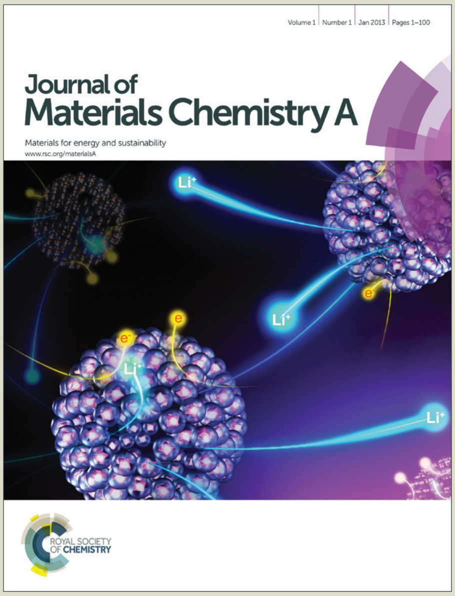

ROYAL SOCIETY OF CHEMISTRY

www.rsc.org/materialsA

Cite this: DOI: 10.1039/c0xx00000x

www.rsc.org/xxxxxx

ARTICLE TYPE

In-situ growth of Co_3O_4 nanoparticles on α-MnO_2 nanotubes: A new hybrid for high-performance supercapacitor

Dongbo Yu,[a,b] Jianfeng Yao,[a] Ling Qiu,[c] Yufei Wang,[c] Xinyi Zhang,[d] Yi Feng,[*b] and Huanting Wang[*a]

Received (in XXX, XXX) Xth XXXXXXXXX 20XX, Accepted Xth XXXXXXXXX 20XX

DOI: 10.1039/b000000x

A new MnO_2@Co_3O_4 hybrid with small-sized Co_3O_4 nanoparticles grown on α-MnO_2 nanotubes was prepared from a low concentration precursor solution by a facile two-step hydrothermal synthesis, and its charge storage properties were investigated by cyclic voltammetry and galvanostatic charge-discharge measurements. Due to its hybrid structure, the well-dispersed Co_3O_4 nanoparticles not only facilitated the charge and ion transfer, but also hindered the dissolution of Mn species, this type of hybrid maximized the electroactivity of both components. The hybrid exhibited a specific capacitance of 234 F/g, which was greater than that of pristine α-MnO_2 nanotubes and physical mixture of α-MnO_2 nanotubes and Co_3O_4 nanoparticles at a current density of 200 mA/g. The hybrid also showed good rate capacity and long-term cycling performance.

1. Introduction

The increasing concerns about the limited fossil fuel supply and global environmental conservation have stimulated considerable research into renewable energy storage and conversion technologies.[1-3] Due to the high power capability, fast charge-discharge rates and excellent cycle lifetime, supercapacitors have attracted extensive attention as it bridges the performance gap between high energy density of battery and high power density of electrolytic capacitor.[4-5] As one of the most promising energy storage technologies, supercapacitors have been used in hybrid electric vehicles, portable electronic devices and backup power.[6-9] In terms of different operating mechanisms, supercapacitors can be normally divided into two types: electrical double-layer capacitances (EDLCs) (i.e., using carbon-based materials including activated carbon, carbon nanotube and graphene etc.)[5, 10-12] and pseudocapacitances (i.e., using transition metal oxide/hydroxide and conductive polymer etc.).[13-17] Unlike the EDLCs stemming from the electrostatic accumulation of charges in the electric double-layer at the interface of electrode and electrolyte, pseudocapacitances store the energy by surface faradic redox reactions generating much higher theoretical capacitance than that of EDLCs. It has been reported that amorphous hydrated RuO_2 can achieve an ultrahigh value of 1340 F/g for specific capacitance (measured at the scan rate of 25 mV/s by cyclic voltammetry).[18] However, despite the remarkable performance of RuO_2, the high cost as well as its toxicity greatly hampers the practical applications. Therefore, some inexpensive transition metal oxides including MnO_2 and Co_3O_4 were employed because of the natural abundance, low cost, environmental friendliness and high theoretical specific capacitance.[19-33]

Owing to the high surface-area utilization, nanosized MnO_2 with different morphology and structure were widely used and thus enhanced the capacitive performance.[19, 28-32] Yu et al. reported the shape-controlled preparation of three-dimensional (3D) hierarchical MnO_2 nanostructures from sea urchin shaped α-MnO_2, α-MnO_2 nanorods clusters and 3D clew-like ε-MnO_2 nanostructures with specific capacitance of 46, 100 and 120 F/g at a scan rate of 5 mV/s, respectively.[19] Zhu et al. fabricated several different MnO_2 tubular nanostructures by using carbonized polyacrylonitrile nanofiber as the sacrificial template in a hydrothermal synthesis.[30] The MnO_2 tubular structures consisting of ultrathin nanosheets showed an enhanced charge storage performance due to its structural features of large specific surface area and interconnected one-dimensional tubular nanostructure, which allows the electrolyte to effectively interact with the active materials and shortens the diffusion paths of the charge carriers.[30] However, the electronic conductivity of MnO_2 is inherently so poor that impedes the charge transfer, then leads to extremely severe reduction of rate capacity.[28, 31] To overcome this drawback, a common strategy is to construct MnO_2-based hybrid capacitors with conductive matrix, such as carbon-based materials,[34-42] conductive polymers [43-45] and ordered nanowire arrays.[46-50] Particularly Fan and co-workers reported a promising route by building up an integrated smart architecture composed of pseudocapacitive metal oxides, in which structural features and electroactivities of each component could fully contribute to the electrochemical energy storage and satisfy the fast ion and electron transfer in the meantime.[49] Their study strongly testified the possibility of designing high-performance pseudocapacitive materials without the use of any carbon- or polymer-based conducting media. Recently, Yang and co-workers designed a new hybrid structure with porous α-Fe_2O_3 branched nanorods well aligned on β-MnO_2 nanorods backbone. The hybrid presented excellent lithium-storage performances that could be assigned to the synergistic effect of different components and the unique structure, suggesting the importance of chemical component selection and the hierarchical structure in the hybrid design.[51]

Therefore, in order to further improve the properties of supercapacitor, it is favourable to fabricate the active materials that take advantages both of the large specific area for high activity and the manipulated structure for fast electron transport and short ion diffusion path. Herein we have successfully prepared a novel hybrid for high-performance supercapacitor by a simple two-step synthesis. In the first step, α-MnO_2 nanotubes were synthesized through a hydrothermal method. The high surface area of α-MnO_2 nanotubes enabled nucleation sites of nanoparticle. In the second step, Co_3O_4 nanoparticles were grown on the surface of α-MnO_2 nanotubes without any pretreatment of α-MnO_2 nanotubes. Both of Co_3O_4 nanoparticles and α-MnO_2 nanotubes could participate into the pseudocapacitive reaction. Owing to the lower resistivity of Co_3O_4, the controlled loading of Co_3O_4 nanoparticles was considered to benefit the charge transfer without affecting the high surface area and the ion penetration into α-MnO_2 nanotube backbone. Such a well-designed hierarchical structure offers effective utilization of active materials, and thus exhibits much better electrochemical performance than that of pure MnO_2 nanotubes and physical mixture of α-MnO_2 nanotubes and Co_3O_4 nanoparticles. This work has demonstrated an alternative approach to constructing supercapacitor materials with high capacitive performance.

2. Experimental section

2.1 Chemicals

Potassium permanganate ($KMnO_4$, ≥ 99.0%), hydrochloric acid (HCl, 37%), cobalt nitrate hexahydrate ($Co(NO_3)_2{\cdot}6H_2O$, ≥ 98%), ammonium fluoride (NH_4F, ≥ 98%), urea ($CO(NH_2)_2$, ≥ 98%), potassium hydroxide (KOH, ≥ 98%), polyvinylidene difluoride (PVDF, average Mw ≈ 534,000), N-methyl-2-pyrrolidone (NMP, ≥ 99.5%), cobalt oxide nanopowder (Co_3O_4, < 50 nm in particle size) and graphitized carbon black (particle size < 200 nm) were purchased from Sigma Aldrich, Australia. All chemicals were used without further purification.

2.2 Synthesis of α-MnO_2 nanotubes

In a typical synthesis, 0.912 g of $KMnO_4$ and 2 ml of HCl (37%) were dissolved in 70 ml of distilled water under magnetic stirring. The precursor solution was then transferred into a 125 ml of Teflon-lined stainless steel autoclave. The autoclave was sealed and kept in an oven at 140 °C for 12 h. After cooling to room temperature naturally, a brown precipitate was washed with distilled water for several times, collected by centrifugation and dried at 80 °C in air overnight. The resulting products were α-MnO_2 nanotubes.

2.3 Synthesis of the hybrids: in situ growth of Co_3O_4 nanoparticles on α-MnO_2 nanotubes

Co_3O_4 nanoparticles were in situ grown on α-MnO_2 nanotubes (denoted as MnO_2@Co_3O_4). 100 mg of as-prepared α-MnO_2 nanotubes were added in 50 ml of aqueous solution containing 0.291 g of $Co(NO_3)_2{\cdot}6H_2O$, 0.3 g of urea and 0.074 g of NH_4F. After ultrasonic treatment for 2 h, the solution was added into a Teflon-lined stainless steel autoclave. The autoclave was heated to 95 °C for 8 h. The resulting material (MnO_2@Co_3O_4-L) was collected by centrifugation, rinsed with water and ethanol and dried at 80 °C in air overnight. For comparison, the hybrid was also prepared at high concentration (MnO_2@Co_3O_4-H) with the precursor solution including 100 mg of α-MnO_2 nanotubes, 0.582 g of $Co(NO_3)_2{\cdot}6H_2O$, 0.6 g of urea and 0.148 g of NH_4F. In addition, the syntheses without adding NH_4F (and α-MnO_2 nanotubes) were also carried out with the same procedures mentioned above. In addition, a physical mixture of 40 mg of Co_3O_4 nanoparticles and 100 mg of α-MnO_2 nanotubes (MnO_2+Co_3O_4) was prepared for electrochemical measurements.

2.4 Characterization

Raman spectra were recorded from an Ar laser (Renishaw Invia) with an excitation line at 514 nm at room temperature. The X-ray diffraction (XRD) was conducted on a Bruker D8 Advance X-ray diffractometer with Cu Kα radiation. The morphology of the composite was examined by field-emission scanning electron microscopy (SEM, JEOL JSM-7100F) and a transmission electron microscope (TEM, JEM-2100) operated at 200 KV.

2.5 Electrochemical measurements

Electrochemistry measurements were investigated by cyclic voltammetry (CV), electrochemical impedance spectroscopy (EIS) and galvanostatic charge-discharge in 1 M KOH solution by using an Autolab 2 instrument. The KCl saturated Ag/AgCl was used as reference electrode, and graphite rod was used as counter electrode. The working electrode for electrochemical measurement was prepared by mixing 80 wt% active material, 10 wt% carbon black and 10 wt% PVDF in NMP solvent. The resulting mixture was placed in an ultrasonic bath for about 1 h to make a homogeneous solution and subsequently dispersed and yielded 0.8 mg/cm^2 of active materials onto 1 cm^2 of carbon paper (TGPH-030, Toray), which was used as current collector rather than Ni foam in our study (The comparison between carbon paper and nickel foam is shown in Fig. S1). Finally, the working electrode was dried in air at 80 °C for 24 h. EIS measurements were tested in the frequency range from 0.1 Hz to 100 kHz at open-circuit potential with an ac perturbation of 0.1 V.

The specific capacitance of the electrode was calculated by Equation 1 (CV curves) and Equation 2 (galvanostatic charge/discharge curves):

$$C_1 = \frac{\int_{V_a}^{V_c} I(V)dV}{mv(V_a - V_c)} \qquad (1)$$

$$C_2 = \frac{I\Delta t}{m\Delta V} \qquad (2)$$

where C_1 and C_2 is the specific capacitance (F/g), m is the mass of the active materials (g), ν is the scan rate of CV curves (V/s), (V_a−V_c) represents the potential window (V), I is the discharge current (A), ΔV is the potential drop excluding the IR drop (V), and Δt is the total discharge time (s).

3. Results and discussion

The component and morphology of α-MnO_2 nanotubes and MnO_2@Co_3O_4 hybrids were examined by XRD, SEM and TEM. As shown in Fig. 1a, the as-synthesized α-MnO_2 nanotubes have tetragonal open ends and the length of individual nanotube is about 1- 3 μm. Fig. 1b clearly shows the nanotubes with outer diameter of about 80 nm and wall thickness of several nanometers. In addition, the diffraction spots shown in the electron diffraction pattern (the left lower corner) indicate the single crystal structure of MnO_2 nanotube, and the lattice spacing of 0.49 nm (the left upper corner inset) corresponds to the (200) planes of the tetragonal α-MnO_2, revealing the growth orientation is along the [100] direction.[52] The XRD pattern of as-synthesized MnO_2 nanotubes (Fig. 2a) can be indexed to the pure tetragonal phase of α-MnO_2 (JCPDS 44-0141), and both of MnO_2@Co_3O_4-H hybrid (Fig. 2b) and MnO_2@Co_3O_4-L hybrid (Fig. 2c) are composed of tetragonal α-MnO_2 phase and face-centered cubic Co_3O_4 phase (JCPDS 42-1467).

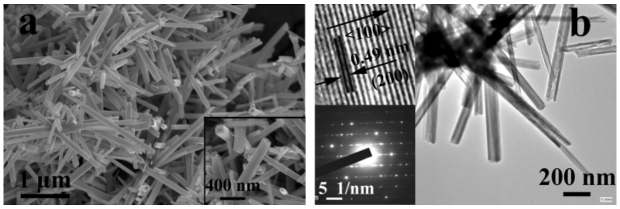

Fig. 1. SEM (a) and TEM (b) images of single-crystal α-MnO_2 nanotubes. The inset in (a) shows the high-magnification image and the insets in (b) show the high-magnification TEM image and corresponding electron diffraction.

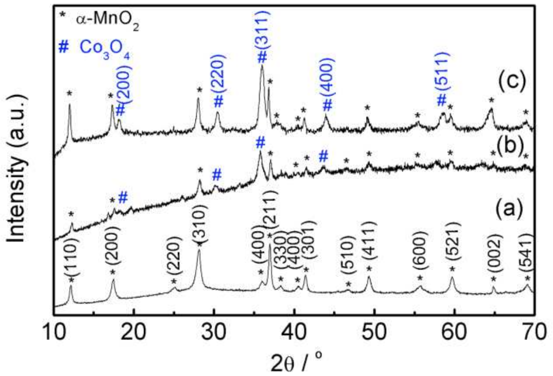

Fig. 2. XRD patterns of α-MnO_2 nanotubes (a), MnO_2@Co_3O_4-H hybrid (b) and MnO_2@Co_3O_4-L hybrid (c).

Fig. 3 shows SEM and TEM images of MnO_2@Co_3O_4 hybrids prepared under low and high concentrations. At the high concentration, MnO_2@Co_3O_4-H hybrid displays a bead-on-string structure with bigger nanoparticles (~120 nm) aligning with the MnO_2 nanotubes (Fig. 3a). However, some bare nanowire clusters or nanoflakes appear when NH_4F is not added, which are marked by arrows in Fig. S2a-c. At the low concentration, the nanotubes are fully covered by small nanoparticles (Fig. 3b). In comparison, in the absence of NH_4F, only a few nanoparticles with sizes of 10-20 nm are dispersed on the side facets of α-MnO_2 nanotubes (Fig. S2d). The TEM image of MnO_2@Co_3O_4-H in Fig. 3c shows the bead-on-string structure and almost no other structural by-products (such as nanowire clusters and nanoflakes) exist. In contrast, very small nanoparticles are uniformly located on the surface of MnO_2 nanotubes for MnO_2@Co_3O_4-L (Fig. 3d and e), although some big nanoparticles with the diameter of ~100 nm are occasionally located on the MnO_2 nanotubes. Jiang et al. pointed out that after introducing F^- anion, Co^{2+} could be gradually released into the reaction system and facilitate the formation of nuclei on substrates, resulting in tight adhesion between Co_3O_4 and substrates.[53] Therefore, it is believed that NH_4F has a great influence on the hybrid synthesis that promotes the nucleation of Co_3O_4 uniformly grown on α-MnO_2 nanotubes. In addition, based on the experimental results, the low concentration of precursor solution facilitates the smaller Co_3O_4 nanoparticles grown on MnO_2 nanotubes, which will benefit the charge storage performance discussed later. The d-spacing values of 0.235, 0.247 and 0.276 nm (Fig. 3f) correspond to the planes of MnO_2 (211), Co_3O_4 $(\bar{1}\bar{1}3)$ and Co_3O_4 (220), respectively, and the crystal orientation perpendicular to the Co_3O_4 particle surfaces is determined as $[1\bar{1}0]$. To further investigate the influence of NH_4F on the morphology of resulting materials, in another experiment, without adding α-MnO_2 nanotubes and NH_4F, the products exhibit a nanowire cluster morphology (Fig. S3a and b) and the related XRD result (Fig. S3c) indicates the nanowire clusters should be $Co(CO_3)_{0.5}(OH)\cdot 0.11H_2O$. Co_3O_4 nanoflakes could be produced in the presence of $Co(NO_3)_2$ and $CO(NH_2)_2$ in the hydrothermal reaction according to the previous study,[26] thus the by-products in the synthesis are considered to result from the fast reaction of $Co(NO_3)_2$ and $CO(NH_2)_2$ if NH_4F is not added. It should be noted that no pre-treatment or post-treatment is required as compared to the preparation of carbon-based materials or the modification of carbon nanotube in the other one-dimensional composites with complex steps.[30, 39, 54-58] Our method possesses significant advantages including simplicity, cost-efficiency and good reproducibility.

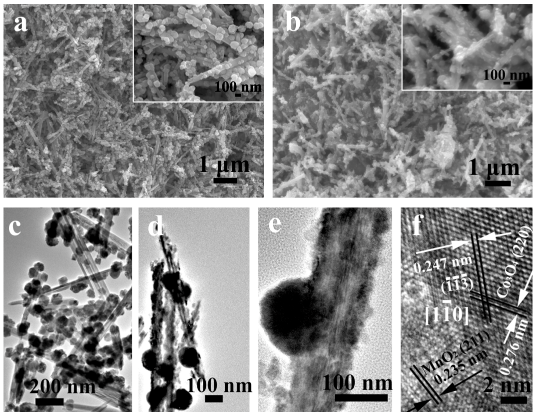

Fig. 3 SEM images of MnO_2@Co_3O_4-H (a) and MnO_2@Co_3O_4-L (b). TEM images of MnO_2@Co_3O_4-H (c), MnO_2@Co_3O_4-L (d, e), and high magnification TEM image of MnO_2@Co_3O_4-L (f). The insets of (a)(b) show the corresponding high-magnification SEM images.

Fig. 4 presents the Raman spectra of α-MnO_2 nanotube, MnO_2@Co_3O_4-H and MnO_2@Co_3O_4-L. For the α-MnO_2 nanotubes, the strong peak of 657 cm^{-1} is attributed to Mn_3O_4 induced in the Ar laser irradiation. The weak peak of 575 cm^{-1} is assigned to the Mn-O lattice vibration in MnO_2, and the weak peaks at 317 and 370 cm^{-1} arise from the formation of Mn_2O_3 or Mn_3O_4 and correspond to the bending mode of Mn-O-Mn.[59] Four new peaks located at 188, 462, 514 and 675 cm^{-1} emerge in the spectrum of $MnO_2@Co_3O_4$-L, which are considered as F_{2g}, E_g, F_{2g} and A_{1g} Raman active modes of Co_3O_4 nanocrystals, respectively.[49] For the $MnO_2@Co_3O_4$-L hybrid, the peak at 575 cm^{-1} becomes stronger and a new peak of 675 cm^{-1} appears as compared to $MnO_2@Co_3O_4$-H. Furthermore, the peak of 657 cm^{-1} related to the laser heating of exposed α-MnO_2 disappears, implying the surface of $MnO_2@Co_3O_4$-L hybrid is fully covered by small-sized Co_3O_4 nanoparticles, which is in good agreement with the SEM and TEM observations. In addition, the Co_3O_4 nanoparticles could form a dense layer to avoid the possible structure deformation and enhance the stability of these supercapacitor materials.[51]

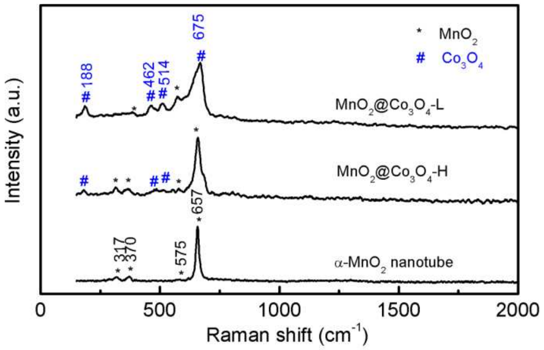

Fig. 4 Raman spectra of α-MnO_2 nanotube, $MnO_2@Co_3O_4$-H and $MnO_2@Co_3O_4$-L.

The electrochemical measurements of α-MnO_2 nanotubes, $MnO_2@Co_3O_4$-H, $MnO_2@Co_3O_4$-L and $MnO_2+Co_3O_4$ were conducted by using a three-electrode configuration on the Autolab 2 instrument in 1 M KOH aqueous solution. Fig. 5a presents the CV plots ranging from 0.1 to 0.5 V at the scan rate of 2 mV/s. The CV of α-MnO_2 nanotubes shows the typical quasi-rectangular shape ascribed to the intercalation/extraction of protons (H_3O^+) or alkali cations (K^+) into the oxide.[46] It could be observed that a pair of redox peaks A/A’ appeared in both of CV plots for $MnO_2@Co_3O_4$-H and $MnO_2@Co_3O_4$-L, which was attributed to the surface Faradic effect described as follows:[21]

$$Co_3O_4 + OH^- + H_2O \leftrightarrow 3CoOOH + e^- \quad (3)$$

$$CoOOH + OH^- \leftrightarrow CoO_2 + H_2O + e^- \quad (4)$$

The specific capacitance (C_1) of α-MnO_2 nanotubes, $MnO_2@Co_3O_4$-H, $MnO_2@Co_3O_4$-L and $MnO_2+Co_3O_4$ calculated from CV plots is 130, 166, 227 and 148 F/g at the scan rate of 2 mV/s, respectively. Both $MnO_2@Co_3O_4$-H and $MnO_2@Co_3O_4$-L hybrids show better charge storage performance than the pristine α-MnO_2 nanotubes and $MnO_2+Co_3O_4$ physical mixture, which should be originated from their specific configurations. On the one hand, the Co_3O_4 nanoparticles of the hybrids directly contribute to the higher capacitance and favour the fast charge transfer resulting from the lower resistivity of Co_3O_4, especially at the high-valance state in charge-discharge process,[60] which can be confirmed by the bigger diameters of semicircles for α-MnO_2 nanotubes and $MnO_2+Co_3O_4$ in Nyquist plots (Fig. 5b). The EIS results also demonstrate no significant function on charge transport as α-MnO_2 nanotubes are physically mixed with Co_3O_4 nanoparticles, leading to the lower specific capacitance of $MnO_2+Co_3O_4$ compared with the $MnO_2@Co_3O_4$ hybrids. On the other hand, compared to the typical CV characterization of pristine Co_3O_4 (overlap in the forward/reverse scan of CV plot at the potential range of 0.1-0.3 V),[49] the CV plots of the two hybrids show rectangular feature as of MnO_2 ranging from 0.1 to 0.3 V (Fig. 5a), which reveals that α-MnO_2 nanotubes are involved in the capacitive reaction. Moreover, $MnO_2@Co_3O_4$-L exhibits the best charge storage performance. In comparison to bead-on-string shaped $MnO_2@Co_3O_4$-H with a bigger Co_3O_4 particle size, $MnO_2@Co_3O_4$-L has the lower charge transfer resistance (Fig. 5b) that benefits the charge transfer and would lead to the superior rate capability of the hybrid. Additionally, since the straight line is ascribed to the diffusive resistance (Warburg impedance) that is related to the electrolyte diffusion within the pores of the electrode, according to the EIS results (Fig. 5b), $MnO_2@Co_3O_4$-L almost has the same diffusion resistance as that of α-MnO_2 nanotubes (parallel to each other at the linear part corresponding to the low frequency range) but better diffusion property than $MnO_2@Co_3O_4$-H. Combining the above SEM and TEM observations (Fig. 3), it is noted that the small Co_3O_4 nanoparticle layer of $MnO_2@Co_3O_4$-L facilitates the ion penetration into α-MnO_2 nanotubes to achieve maximized utilization of pseudocapacitive materials due to the slightly bigger circled area of rectangle part for $MnO_2@Co_3O_4$-L (at the potential range of 0.1-0.3 V in Fig. 5a). Upon increasing the scan rate to 50 mV/s, the oxidation peaks of the hybrids positively shift and the reduction peaks shift negatively (Fig. S4a-c). The current density of active materials increases while the specific capacitance reduces with the increase of scan rate as shown in Table 1. The capacitance remains at 75.3% for $MnO_2@Co_3O_4$-L when the scan rate was varied from 2 to 50 mV/s, indicating $MnO_2@Co_3O_4$-L had a better rate capability than that of $MnO_2@Co_3O_4$-H (65.8%), α-MnO_2 nanotubes (65.4%) and $MnO_2+Co_3O_4$ (65.5%).

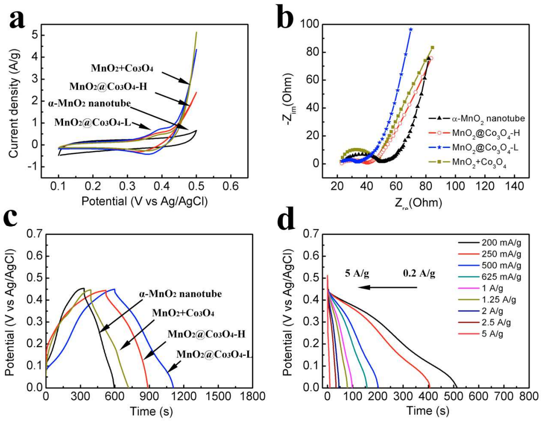

Fig. 5 Electrochemical properties of α-MnO_2 nanotube, $MnO_2@Co_3O_4$-H, $MnO_2@Co_3O_4$-L and $MnO_2+Co_3O_4$ in 1 M KOH aqueous solution: (a) CVs at the scan rate of 2 mV/s; (b) Nyquist plots at the range of 0.1 Hz-100 KHz; (c) galvanostatic charge-discharge curves at a current density of 200 mA/g; (d) galvanostatic discharge curves of $MnO_2@Co_3O_4$-L at different current densities.

Table 1 Specific capacitance values of α-MnO_2 nanotube, MnO_2@Co_3O_4-H, MnO_2@Co_3O_4-L and MnO_2+Co_3O_4.

Scan rate (mV/s)	Specific capacitance (F/g)			
	α-MnO_2 nanotube	MnO_2@Co_3O_4-H	MnO_2@Co_3O_4-L	MnO_2+ Co_3O_4
2	130	166	227	148
5	115	148	216	138
10	108	141	203	129
20	98	126	192	114
50	85	109	171	97

The pseudocapacitive property was further estimated by galvanostatic charge–discharge measurements. As shown in Fig. 5c, MnO_2@Co_3O_4-L displays the highest specific capacitance at the current density of 200 mA/g, it exhibits pseudocapacitance (C_2) of 234 F/g at 0.2 A/g, 229 F/g at 0.5 A/g, 220 F/g at 1 A/g, 209 F/g at 2 A/g, 176 F/g at 5 A/g (Fig. 5d) and shows good capacitance retention of 89.3% with increasing the current density from 0.2 A/g to 2 A/g. These obtained specific capacitance and rate capability values are higher than those reported MnO_2-based composites incorporated with carbon- or conductive polymer-based materials, such as graphene-wrapped/MnO_2 composites (210 F/g at 0.5 A/g, 70% retention at 5 A/g),[54] nitrogen-doped graphene/ultrathin MnO_2 sheet composites (257.1 F/g at 0.2 A/g, 74.8% retention at 2 A/g),[61] graphene oxide/needle-like MnO_2 composites (197.2 F/g at 0.2 A/g, 56.4% retention at 1 A/g) [38] and mesoporous carbon/MnO_2 composites (205 F/g at 0.2 A/g, 70% retention at 1A/g),[62] suggesting this well-designed hybrid offers an excellent charge storage performance even though all of the components are pseudocapacitive metal oxides. Fig. 6a shows the summary plots of specific capacitance values from Fig. 5d, Fig. S4d and e. The loss of capacitance follows the order: α-MnO_2 nanotube > MnO_2+Co_3O_4 > MnO_2@Co_3O_4-H > MnO_2@Co_3O_4-L in agreement with the CV results by changing the scan rate, which indicates the better rate capability of MnO_2@Co_3O_4-L. Besides the improved specific capacitance and good rate capability, the unique hybrid structure performs outstanding cycling stability. Fig. 6b shows the charge-discharge cycles at a constant current density of 2 A/g in 1 M KOH electrolyte solution. MnO_2@Co_3O_4-L can still retain 87.5% of capacitance value after 2000 cycles compared with 80.8% for α-MnO_2 nanotubes, 77.6% for MnO_2@Co_3O_4-H and 77.8% for MnO_2+Co_3O_4. In the charge/discharge process, the intercalation/extraction of ions into the active materials causes the electrode stress due to their different expansion coefficient, which may greatly weaken the connection between Co_3O_4 nanoparticles and α-MnO_2 nanotubes, and then result in the big electronic resistance of electrode.[35, 63] In addition, directly mixing α-MnO_2 nanotubes with Co_3O_4 nanoparticle results in less improvement in conductivity (Fig. 5b). MnO_2@Co_3O_4-H shows the close loss of capacitance of MnO_2+Co_3O_4, thus the superior cycling performance of MnO_2@Co_3O_4-L demonstrates that the thinner Co_3O_4 nanoparticles loaded on α-MnO_2 nanotubes could give rise to better structural integrity of hybrids than bigger nanoparticles for MnO_2@Co_3O_4-H. Furthermore, the very thin Co_3O_4 nanoparticles can generate a protective layer on the surface of α-MnO_2 nanotubes to prevent the Mn species from dissolving in the electrolyte solution, thus MnO_2@Co_3O_4-L shows better cycling stability than α-MnO_2 nanotubes .[51]

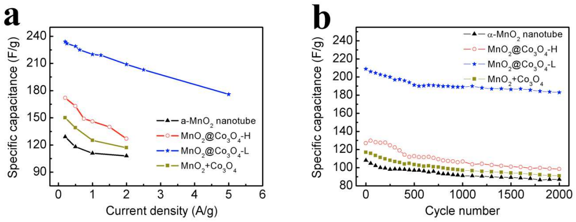

Fig. 6 Summary plots of specific capacitance value at different current densities (a) and the cycling performance at a current density of 2 A/g (b) of α-MnO_2 nanotube, MnO_2@Co_3O_4-H, MnO_2@Co_3O_4-L and MnO_2+Co_3O_4 in 1 M KOH aqueous solution.

4. Conclusions

We have synthesized a novel hybrid composed of α-MnO_2 nanotubes and Co_3O_4 nanoparticles by a simple hydrothermal method without involving any surfactants or surface modifications. The addition of NH_4F and the concentration of precursor solution play important roles in the synthesis. MnO_2@Co_3O_4-H prepared with a high concentration precursor solution shows a bead-on-string morphology with big Co_3O_4 nanoparticles distributed on α-MnO_2 nanotubes. For the MnO_2@Co_3O_4-L prepared at a low concentration precursor solution, the surface of α-MnO_2 nanotube is fully covered by the small-sized Co_3O_4 nanoparticles that could improve the charge transfer property, hinder the dissolution of Mn species and allow the ion transport into the backbone. Therefore, both α-MnO_2 nanotubes and smaller Co_3O_4 nanoparticles of MnO_2@Co_3O_4-L display enhanced electroactivity for charge storage. Owing to the unique structure, the specific capacitance and rate capacity of MnO_2@Co_3O_4-L are better than those of α-MnO_2 nanotubes, MnO_2@Co_3O_4-H and MnO_2+Co_3O_4. In addition, MnO_2@Co_3O_4-L can retain 87.5% of capacitance after 2000 charge-discharge cycles. In conclusion, this well-designed hybrid exhibits an excellent energy storage property, which suggests an alternative way of constructing high-performance supercapacitors without using carbon- or polymer-based conductive materials.

Acknowledgements

This work was financially supported by the Australian Research Council. D.Y. would like to thank China Scholarship Council and Department of Chemical Engineering at Monash University for hosting his visiting study. H.W. is a recipient of an Australian Research Council Future Fellowship (project no. FT100100192). J.Y. thanks Monash University for the Monash Fellowship.

Notes and references

[a] *Department of Chemical Engineering, Monash University, Clayton, Victoria 3800, Australia; E-mail: huanting.wang@ monash.edu (H. Wang)*
[b] *School of Materials Science and Engineering, Hefei University of Technology, Hefei, Anhui 230009, People's Republic of China; E-mail: fyhfut@126.com (Y. Feng)*
[c] *Department of Materials Engineering, Monash University, Clayton, Victoria 3800, Australia*
[d] *School of Chemistry, Monash University, Clayton, Victoria 3800, Australia*

† Electronic Supplementary Information (ESI) available: [Comparison between carbon paper and nickel foam; SEM and TEM images of MnO_2@Co_3O_4 composites without NH_4F; SEM images and XRD pattern

of the products without the addition of α-MnO$_2$ nanotubes and NH$_4$F; Cyclic voltammetric curves at different scan rates and galvanostatic discharge curves at different current densities.]. See DOI: 10.1039/b000000x/

1 B. Tian, X. Zheng, T. J. Kempa, Y. Fang, N. Yu, G. Yu, J. Huang and C. M. Lieber, *Nature*, 2007, **449**, 885-889.
2 C. K. Chan, H. Peng, G. Liu, K. McIlwrath, X. F. Zhang, R. A. Huggins and Y. Cui, *Nat. Nanotechnol.*, 2007, **3**, 31-35.
3 M. Winter, *Chem. Rev.*, 2004, **104**, 4245–4270.
4 P. Simon and Y. Gogotsi, *Nat. Mater.*, 2008, **7**, 845 - 854
5 Y. Zhai, Y. Dou, D. Zhao, P. F. Fulvio, R. T. Mayes and S. Dai, *Adv. Mater.*, 2011, **23**, 4828-4850.
6 D. N. Futaba, K. Hata, T. Yamada, T. Hiraoka, Y. Hayamizu, Y. Kakudate, O. Tanaike, H. Hatori, M. Yumura and S. Iijima, *Nat. Mater.*, 2006, **5**, 987-994.
7 R. Liu, J. Duay and S. B. Lee, *Chem. Commun.*, 2011, **47**, 1384–1404.
8 P. J. Hall, M. Mirzaeian, S. I. Fletcher, F. B. Sillars, A. J. R. Rennie, G. O. Shitta-Bey, G. Wilson, A. Cruden and R. Carter, *Energy Environ. Sci.*, 2010, **3**, 1238–1251.
9 A. Du Pasquier, I. Plitz, S. Menocal and G. Amatucci, *J. Power Sources*, 2003, **115**, 171-178.
10 J. Wang and S. Kaskel, *J. Mater. Chem.*, 2012, **22**, 23710–23725.
11 G. Xu, C. Zheng, Q. Zhang, J. Huang, M. Zhao, J. Nie, X. Wang and F. Wei, *Nano Res.*, 2011, **4**, 870-881.
12 E. Raymundo-Piñero, F. Leroux and F. Béguin, *Adv. Mater.*, 2006, **18**, 1877-1882.
13 J. Duay, S. A. Sherrill, Z. Gui, E. Gillette and S. B. Lee, *ACS Nano*, 2013, **7**, 1200–1214.
14 M. Zhi, C. Xiang, J. Li, M. Li and N. Wu, *Nanoscale*, 2013, **5**, 72–88.
15 C. Zhou, Y. Zhang, Y. Li and J. Liu, *Nano Lett.*, 2013, **13**, 2078-2085.
16 W. Deng, X. Ji, Q. Chen and C. E. Banks, *RSC Adv.*, 2011, **1**, 1171–1178.
17 H. Zhou, L. Liu, X. Wang, F. Liang, S. Bao, D. Lv, Y. Tang and D. Jia, *J. Mater. Chem. A*, 2013, **1**, 8525–8528.
18 C.-C. Hu, W.-C. Chen and K.-H. Chang, *J. Electrochem. Soc.*, 2004, **151**, A281-A290.
19 P. Yu, X. Zhang, D. Wang, L. Wang and Y. Ma, *Cryst. Growth Des.*, 2009, **9**, 528–533.
20 Y. Wang, Z. Zhong, Y. Chen, C. T. Ng and J. Lin, *Nano Res.*, 2011, **4**, 695-704.
21 D. Wang, Q. Wang and T. Wang, *Inorg. Chem.*, 2011, **50**, 6482-6492.
22 Z. Yu, B. Duong, D. Abbitt and J. Thomas, *Adv. Mater.*, 2013, **25**, 3302-3306.
23 G. X. Pan, X. H. Xia, F. Cao, P. S. Tang and H. F. Chen, *Electrochem. Commun.*, 2013, **34**, 146-149.
24 B. Wang, T. Zhu, H. B. Wu, R. Xu, J. S. Chen and X. W. Lou, *Nanoscale*, 2012, **4**, 2145–2149.
25 Y. Xiao, A. Zhang, S. Liu, J. Zhao, S. Fang, D. Jia and F. Li, *J. Power Sources*, 2012, **219**, 140-146.
26 S. K. Meher and G. R. Rao, *J. Phys. Chem. C*, 2011, **115**, 15646-15654.
27 T. Zhu, J. S. Chen and X. W. Lou, *J. Mater. Chem.*, 2010, **20**, 7015–7020.
28 V. Subramanian, H. Zhu and B. Wei, *J. Power Sources*, 2006, **159**, 361-364.
29 H. Xia, J. Feng, H. Wang, M. O. Lai and L. Lu, *J. Power Sources*, 2010, **195**, 4410-4413.
30 J. Zhu, W. Shi, N. Xiao, X. Rui, H. Tan, X. Lu, H. H. Hng, J. Ma and Q. Yan, *ACS Appl. Mater. Interfaces*, 2012, **4**, 2769-2774.
31 W. Xiao, H. Xia, J. Y. H. Fuh and L. Lu, *J. Power Sources*, 2009, **193**, 935-938.
32 M. Xu, L. Kong, W. Zhou and H. Li, *J. Phys. Chem. C*, 2007, **111**, 19141 - 19147.
33 V. Subramanian, H. Zhu and B. Wei, *Electrochem. Commun.*, 2006, **8**, 827-832.
34 J.-G. Wang, Y. Yang, Z.-H. Huang and F. Kang, *J. Power Sources*, 2013, **224**, 86-92.
35 Y. Jin, H. Chen, M. Chen, N. Liu and Q. Li, *ACS Appl. Mater. Interfaces*, 2013, **5**, 3408-3416.
36 J. Liu, J. Essner and J. Li, *Chem. Mater.*, 2010, **22**, 5022-5030.
37 Z.-S. Wu, W. Ren, D.-W. Wang, F. Li, B. Liu and H.-M. Cheng, *ACS Nano*, 2010, **4**, 5835–5842.
38 S. Chen, J. Zhu, X. Wu, Q. Han and X. Wang, *ACS Nano*, 2010, **4**, 2822–2830.
39 H. Zheng, J. Wang, Y. Jia and C. a. Ma, *J. Power Sources*, 2012, **216**, 508-514.
40 Y. Peng, Z. Chen, J. Wen, Q. Xiao, D. Weng, S. He, H. Geng and Y. Lu, *Nano Res.*, 2010, **4**, 216-225.
41 G. Yu, L. Hu, N. Liu, H. Wang, M. Vosgueritchian, Y. Yang, Y. Cui and Z. Bao, *Nano Lett.*, 2011, **11**, 4438-4442.
42 X. M. Feng, Z. Z. Yan, N. N. Chen, Y. Zhang, Y. W. Ma, X. F. Liu, Q. L. Fan, L. H. Wang and W. Huang, *J. Mater. Chem. A*, 2013, **1**, 12818-12825.
43 Y. Hou, Y. Cheng, T. Hobson and J. Liu, *Nano Lett.*, 2010, **10**, 2727-2733.
44 R. Liu and S. B. Lee, *J. Am. Chem. Soc.*, 2008, **130**, 2942 - 2943.
45 F. J. Liu, *J. Power Sources*, 2008, **182**, 383-388.
46 J. Cao, M. Safdar, Z. Wang and J. He, *J. Mater. Chem. A*, 2013, DOI: 10.1039/c1033ta12012k.
47 J. Duay, S. A. Sherrill, Z. Gui, E. Gillette and S. B. Lee, *ACS Nano*, 2013, **7**, 1200–1214.
48 P. Yang, X. Xiao, Y. Li, Y. Ding, P. Qiang, X. Tan, W. Mai, Z. Lin, W. Wu, T. Li, H. Jin, P. Liu, J. Zhou, C. P. Wong and Z. L. Wang, *ACS Nano*, 2013, **7**, 2617–2626.
49 J. Liu, J. Jiang, C. Cheng, H. Li, J. Zhang, H. Gong and H. J. Fan, *Adv. Mater.*, 2011, **23**, 2076-2081.
50 S. Dong, X. Chen, L. Gu, X. Zhou, L. Li, Z. Liu, P. Han, H. Xu, J. Yao, H. Wang, X. Zhang, C. Shang, G. Cui and L. Chen, *Energy Environ. Sci.*, 2011, **4**, 3502–3508.
51 X. Gu, L. Chen, Z. Ju, H. Xu, J. Yang and Y. Qian, *Adv. Funct. Mater.*, 2013, **23**, 4049–4056.
52 J. Luo, H. T. Zhu, H. M. Fan, J. K. Liang, H. L. Shi, G. H. Rao, J. B. Li, Z. M. Du and Z. X. Shen, *J. Phys. Chem. C*, 2008, **112**, 12594-12598.
53 J. Jiang, J. P. Liu, X. T. Huang, Y. Y. Li, R. M. Ding, X. X. Ji, Y. Y. Hu, Q. B. Chi and Z. H. Zhu, *Cryst. Growth Des.*, 2010, **10**, 70-75.
54 J. Zhu and J. He, *ACS Appl. Mater. Interfaces*, 2012, **4**, 1770-1776.
55 C. Xiang, M. Li, M. Zhi, A. Manivannan and N. Wu, *J. Power Sources*, 2013, **226**, 65-70.
56 M. Xu, F. Wang, Y. Zhang, S. Yang, M. Zhao and X. Song, *Nanoscale*, 2013, **5**, 8067-8072.
57 Z. Chen, Y. Qin, D. Weng, Q. Xiao, Y. Peng, X. Wang, H. Li, F. Wei and Y. Lu, *Adv. Funct. Mater.*, 2009, **19**, 3420-3426.
58 L. S. Aravinda, K. K. Nagaraja, H. S. Nagaraja, K. U. Bhat and B. R. Bhat, *Electrochim. Acta*, 2013, **95**, 119-124.
59 F. Buciuman, F. Patcas, R. Craciun and D. R. T. Zahn, *Phys. Chem. Chem. Phys.*, 1999, **1**, 185-190.
60 D. Yu, X. Zhang, K. Wang, L. He, J. Yao, Y. Feng and H. Wang, *Int. J. Hydrogen Energy*, 2013, **38**, 11863–11869.
61 S. Yang, X. Song, P. Zhang and L. Gao, *ACS Appl. Mater. Interfaces*, 2013, **5**, 3317-3322.
62 Y. Peng, Z. Chen, J. Wen, Q. Xiao, D. Weng, S. He, H. Geng and Y. Lu, *Nano Res.*, 2011, **4**, 216-225.
63 S. B. Bubenhofer, C. M. Schumacher, F. M. Koehler, N. A. Luechinger, G. A. Sotiriou, R. N. Grass and W. J. Stark, *ACS Appl. Mater. Interfaces*, 2012, **4**, 2664-2671.

TOC

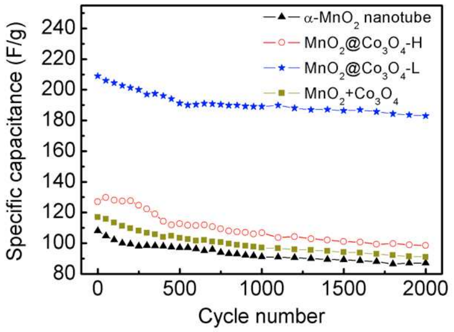

A new MnO$_2$@Co$_3$O$_4$ hybrid with small-sized Co$_3$O$_4$ nanoparticles grown on α-MnO$_2$ nanotubes exhibited much improved specific capacitance than pristine α-MnO$_2$ nanotubes and the physical mixture of α-MnO$_2$ nanotubes and Co$_3$O$_4$ nanoparticles, and also showed good rate capacity and long-term cycling performance.